Mechanistic insights into removal of norfloxacin from water using different natural iron ore – biochar composites: more rich free radicals derived from natural pyrite-biochar composites than hematite-biochar composites

Xing Yang, Xiaoli Zhang, Zhaowei Wang*, Shan Li, Jing Zhao, Guiwei Liang, Xiaoyun Xie

Gansu Key Laboratory for Environmental Pollution Prediction and Control, College of Earth and Environmental Sciences, Lanzhou University, Lanzhou, 730000, China

A B S T R A C T

Two novel magnetic hematite-biochar composites (FOC) and pyrite-biochar composites (FSC) were successfully fabricated through co-pyrolysis as low-cost materials to remove norfloxacin (NOR) from aqueous solution. Multiple characterization results revealed that natural hematite and natural pyrite were successfully loaded on the surface of biochars respectively. After introducing Fe and S, the removal performance of FSC was better than that of FOC and primitive biochar (BC). This was not only due to the increase of the average pore width and abundant surface functional groups, but also since that $\cdot OH$ and $SO_4 \cdot^-$ played the key role in the removal of NOR, which was confirmed by Election Paramagnetic Resonance (EPR) experiments. High Resolution Mass Spectrometer (HRMS) was used to determine the transformation intermediates of NOR and the possible degradation pathways were proposed. Excellent adsorption performance and free radicals ($\cdot OH$ and $SO_4 \cdot^-$) action made FSC had the best removal performance on NOR in this study.

1. Introduction

Among the various pharmaceutical compounds, antibiotics, as emerging pollutants, have received growing concern because of the omnipresent occurrence and ecological risks for the past few years. There are many types of antibiotics, of which fluoroquinolones antibiotics (FQAs) are widely used to treat bacterial infections in humans and other animals, livestock and aquaculture in recent years, and can inhibit DNA replication and transcription with a broad spectrum of antimicrobial properties [1]. Continuous release of FQAs into the aquatic environment might induce the production of antibiotic resistant genes and bacteria [2]. The possible detrimental side effects of the presence of FQAs in the environment are not fully understood but are known to be toxic to plants and aquatic organisms [3]. Meanwhile, due to the poor stability and biodegradability of quinolone rings, most FQAs could not be effectively removed by conventional microbiological methods in sewage treatment plants [4]. A research has shown that quinolone antibiotics accounted for almost 30 million antibiotic prescriptions in the United States in 2016 [5]. Therefore, it is of great importance to seek highly efficient technologies to remove FQAs in water [6]. Especially norfloxacin (NOR), the second most frequently detected antibiotic among fluoroquinolones, has been detected at relatively high levels in various water matrices such as wastewater effluents, surface water and even drinking water [7]. At present, there are a variety of treatment methods to remove diverse pollutants in water, including photocatalytic degradation, adsorption, electrochemical, Fenton oxidation method and so on. As a member of advanced oxidation processes (AOPs) category, photocatalytic degradation is generally based on the combination of semiconductor and light irradiation to degrade pollutants successfully [8–11]. In similar photocatalytic degradation reactions, electron holes [12], superoxide radicals ($\cdot O_2^-$) [13] and hydroxyl radicals ($\cdot OH$) [14] played the key role in the degradation of pollutants. Taking a full consideration of the characteristics of free radicals in the degradation of pollutants, it is very important to introduce free radicals into the reaction system to remove pollutants. The focus of this paper was on exploring an economical and green material, which can remove NOR effectively and conveniently in water based on the combination of the adsorption performance and free radicals catalytic performance of the material.

Biochars are the carbonaceous material prepared from agricultural wastes, industrial organic wastes and forestry wastes [15,16], which were produced via the pyrolysis of massive biomass and the main sources of biochars preparation are as follows: coconut shell [17], rice husk [18], swine manure [19] and so on. Due to its high surface area, porous structure, abundant functional groups and acid and alkali corrosion resistance, biochars have been widely studied and applied in the

field of pollutants removal and wastewater purification [15], such as diverse organic contaminants (e.g., antibiotics [20], bisphenol A [21], aromatic dyes [22]), and a series of inorganic contaminants (e.g., heavy metals [23]) from aqueous, gaseous and/or solid phases. However, due to its low adsorption capacity, the limited types of surface functional groups and low anti-interference ability, the original biochars always failed to reach the needs of actual wastewater treatment [24]. In order to overcome the defects and deficiencies of original biochars, researches and applications on biochars are mainly focused on adjusting the structures and properties of biochar by activating or introducing functional groups to improve its removal effect on organic and inorganic pollutants in recent years [25]. Liu et al. made rice husk waste resources as raw materials, as well as used acid and alkali modification methods to optimize the performance of the original biochars, the results showed that after alkali modification, biochars improved significantly adsorption ability of tetracycline (TC) in the wastewater, on account of its larger specific surface area and increased surface functional groups [26]. Reguyal et al. mixed with pine sawdust and $FeCl_2$ to prepare magnetic biochar composites to adsorption sulfamethoxazole because of the larger average pore and richer surface-active action [27]. Zhou's related researches were about doping Fe/Zn to modify sawdust biochars to conduct simultaneous treatment of tetracycline (TC) and Cu (II) polluted water [28].

Reeds are one kind of the gramineous plant, which are mainly growth in irrigation ditch, river embankment marshland and so on, which have been used as biomass in recent years [29,30]. Hematite is the most stable mineral facies in soil iron oxide, and one of the most important and common iron oxide minerals in highly weathered soils such as red soil, brick red soil and dry red soil. Pyrite, one of the most common species of sulfur-containing minerals on earth, has been recognized as efficient oxidants activators for contaminants degradation and water disinfection because of its high abundance, low material costs [31] and the reduction potential of both Fe(II) and S_2^{2-} [32,33]. Therefore, it could be considered to prepare a kind of composite materials combining the advantages of original biochars and natural iron ore, using its larger specific surface area or pore width, and the ability of producing active groups or free radicals to promote the degradation of pollutants. However, there are few studies on this subject.

Hence, the objectives of this work include: i) the preparation of two novel types of iron based biochar composites with making full use of the advantages of biochars and two kinds of natural iron ore; ii) the researches of the differences of structures and characteristics of hematite-biochar composites (FOC) and pyrite-biochar composites (FSC), as well as, the removal performance and influence factors to NOR; and iii) elucidate the removal mechanism of NOR, the role of sulfide, free radicals or related conversion intermediates in reaction system by using Scanning Electron Microscopy (SEM), Transmission Electron Microscopy (TEM), Electron Paramagnetic Resonance (EPR), the X-ray Photoelectron Spectroscopy (XPS), and High Resolution Mass Spectrometer (HRMS).

2. Material and methods

2.1. Reagents

Norfloxacin (NOR, $C_{16}H_{18}FN_3O_3$, purity > 98.0%, molar mass 319.33 g/mol, CAS Number: 70458-96-7, and the molecular structure is shown in Figure S1) was purchased from the Sigma Chemical Company. All other chemicals used in these experiments were analytical grade (purity > 99%). Pyrite was obtained from Hull Mining Products co. LTD from Tongling city, Anhui Province of China and the S and Fe contents of pyrite were 47.28% and 43.23% respectively and hematite ($Fe_2O_3 \geq 85\%$) was obtained from JinPeng Friction Material co. LTD from Daye city, Hubei Province of China. Deionized (DI) water (18.2 $M\Omega\,cm$) was used for all experiments.

Reed straw were taken from Lanzhou (GanSu, China) reach of

Yellow River, chopped with a plant crusher and then sieved through a 20-mesh screen prior to use.

2.2. Preparation of different materials

Reed straw biochars (BC) were prepared in the muffle furnace with the pyrolysis temperature of 500 °C for 5 h under the oxygen-limited conditions [34]. Meanwhile, adapting a modified method described by our previous study to prepared pyrite-biochar composites (FSC) and hematite-biochar composites (FOC) [35]. Firstly, after the preliminary experiments, the ratio of iron ore to biomass was 1:3. Briefly, corresponding proportion of pyrite or hematite powder and biomass were mixed with deionized (DI) water, sonicated with ultra sonicator, and magnetic stirred constantly for 2 h. Then, the mixture sample was oven-drying at 80 °C and then pyrolyzed at 600 °C for 6 h in the muffle furnace under the oxygen-limited conditions. After cooling to the room temperature, FSC and FOC were washed several times to reach pH equilibrium, dried at 80 °C, ground, passed through a 100-mesh screen and stored for further investigations.

2.3. Characterization methods

The BET specific surface area, total pore volume and average pore width of BC, FOC and FSC were determined by the Brunauer-Emmett-Teller (BET) method and Barrett-Joyner-Halenda (BJH) method (Tristar II 3020, Micromeritics Instrument, USA). The surface morphology and elemental composition of these materials were characterized by scanning electron microscopy (SEM, JSM-5600LV, JEOL, Japan) and energy dispersive spectrometer (EDS, IE250, Oxford Instrument, UK) and obtained surface elemental distribution maps. The morphology and size of different materials were examined by transmission electron microscopy (TEM, TECNAIG², FEI, USA). Functional groups (FGs) on the surface of FSC and FOC before and after reaction were obtained via Fourier transform infrared spectroscopy (FTIR, Nexus 670, Thermo-Nicolet, USA). The X-ray diffraction meter (XRD, D/max-2400, Rigaku, Japan) was used for the confirmation of the structure and crystallinity of the BC, FOC and FSC. Magnetic property of FOC and FSC were characterized with vibrating sample magnetometer (VSM, MicroSense EV-9, USA). The full spectrum analyses of these materials were performed by the X-ray photoelectron spectroscopy (XPS, AXIS Ultra DLD, Japan) with high resolution spectral binding energy. The total organic carbon (TOC) of different samples were determined on a TOC analyzer (Elementar vario TOC select).

The pH drift method was used to identify the point of zero charge pH (pH_{pzc}) of FOC and FSC [36]. Different materials were put in 25 ml of 0.01 M $CaCl_2$ solution respectively. The initial pH values (pH_i) were adjusted in the range of 2.0–11.0 by adding 0.1 M HCl or NaOH, then the solution were shaken at 25 °C under the dark conditions for 24 h. The pH values of the suspensions (pH_f) were determined after centrifugal and filtration. The difference between the pH_f and pH_i were plotted against pH_i [37].

Election paramagnetic resonance (EPR) experiments were performed on a Bruker A300-9.5/12 (Germany) spectrometer using 5.5-dimethyl-1-pyrroline N-oxide (DMPO) as the spin-trapping agent. HRMS (Orbitrap Elite, Velos Pro, Thermo Scientific, USA) was used for the identification of degradation intermediates of NOR and the positive electrospray ionization mode over a mass range of 100–330 m/z was applied to conduct mass spectroscopy.

3. Experimental procedure

To investigate the removal ability and differences of FOC and FSC for NOR, the batch removal experiments were conducted. Through the preliminary experiment, the optimal dosage was determined to be 0.1 g (Figure S2). The removal kinetics were investigated at different time intervals. Meanwhile, the adsorption isotherms at 15 °C, 25 °C and 35 °C

were conducted with different initial NOR concentrations ranging from 2 mg/L to 30 mg/L with the same pH of 7.0 ± 0.05. Furthermore, the effects of initial solution pH and common ion strength (Ca^{2+}) were investigated. Finally, the solution were filtered, and analyzed at 271 nm by using the UV–vis spectrophotometer (Unicam UV300, Thermo Spectronic, USA).

The removal rate (R, %) and adsorption capacity (Q_e, mg/g) of NOR by the materials were calculated as follows:

$$R = \frac{C_0 - C_t}{C_0} \times 100\% \tag{1}$$

$$Q_e = \frac{(C_0 - C_t)V}{m} \tag{2}$$

where C_0 (mg/L) and C_t (mg/L) are the initial and equilibrium concentration of NOR solution respectively; m (g) is the mass of the materials; V (L) is the volume of solution.

4. Results and discussion

4.1. Characterizations of materials

As generalized in Table 1, the yields of FOC and FSC greatly increased after introducing natural hematite and pyrite. On the contrary, the corresponding values of BET specific surface area and total pore volume decreased, especially for FSC, which were might be due to the composite materials contain considerable proportion of iron oxide and iron sulfide, resulting in small surface areas and blocking the pores [38]. Additionally, it was worth noting that the differences of values of average pore width, the addition of the natural mineral increased the average pore width of pristine biochars, especially for FSC, the average pore width of it was about 1.8 times larger than that of BC. Because of the presence of more mesoporous cells on the composites [39], it facilitated the diffusion of antibiotic molecules to the surface and interior of the FSC [40]. Therefore, it can be speculated that the average pore width was the main reason to determine the adsorption capacity of these materials.

As depicted in Table 1, the major element contents of BC were C, O, Si, and the element contents of Mg, Al, Ca, Fe, S of FOC and FSC were appeared after introducing natural hematite and pyrite, which were mainly on account of the introduction of element composition of the natural hematite and pyrite with the chemical composition $MgFeAlO_4$ and $Fe_2(SO_4)_3$, respectively. In addition, the element contents of O of FOC and FSC were lower than that of BC. The morphologies and microstructures of these materials were observed by SEM and TEM images. As shown in the Fig. 1 (a), (b), rod structure with a disorganized and disordered mesoporous structures that still contained the reed straw' original morphology, and it could be clearly observed from Fig. 1 (c) and (d) that the FOC and FSC surface was covered by a layer of film, which brought about rougher surface than BC. This might be attributed to the presence of iron oxide particles and iron sulfide particles adhered on the surface of the rod. TEM images further confirmed that the obtained FOC (Fig. 2 (a) and (b)) and FSC (Fig. 2 (c) and (d)) were rod structure with many fine particles on the surface, which were consistent with the results of SEM. The EDS spectrum graphs of FOC and FSC were shown in Fig. 2 (e), (f), after the addition of hematite and

pyrite, the presence of Fe and S were verified by the corresponding peaks. These results were further evidenced the hematite-biochar and pyrite-biochar composites were prepared successfully.

Fourier Transform Infrared (FTIR) spectra of BC, FOC and FSC were conducted to confirm the functional groups (Fig. 3). For BC, the peaks at 3426, 1588, 1099, 807 and 465 cm^{-1} were ascribed to the stretching vibration of −OH, C=C, C−O, C−H and Si−O [41–44]. Compared with BC, the peaks of FSC and FOC at 3426 cm^{-1} (−OH), 1588 cm^{-1} (C=C), 1099 cm^{-1} (C−O) and 456 cm^{-1} (Si−O) were all diminished. Except the above shared characterization peaks, the new characteristic peaks of FOC and FSC at about 695 and 561 cm^{-1} were assigned to the stretching vibration of Fe-O group [43,45], which were attributed to the formation of iron oxides. According to results mentioned above, the introduction of Fe−O group and the changes of other functional groups were be confirmed that the composite materials were prepared successfully.

Learning from Fig. 4, as for FOC, the XRD patterns displayed five sharp characteristic peaks of γ-Fe_2O_3 at 2θ values of 30.36°, 35.74°, 43.47°, 57.51° and 63.17° [46], corresponding to the (220), (311), (400), (511) and (440) magnetite's crystal planes respectively. In addition, the peaks at 20.87° and 26.65° might be ascribed to SiO_2 and the 50.01° and 68.25° might be corresponded to Fe_3O_4. XRD patterns of FSC displayed three sharp characteristic peaks of Fe_3O_4 at 35.52°, 56.96° and 62.70° [47], corresponding to the (311), (333) and (440) magnetite's crystal planes respectively. Because of the introduction of natural pyrite, the additional peaks at 20.79°, 26.53° and 33.08°, 37.11°, 47.42° might be ascribed to $Fe_2(SO_4)_3$, and FeS_2 respectively [48]. The XRD analysis showed that the biochars surface were successfully loaded with hematite and pyrite respectively, and demonstrated that with the addition of the element of Fe, both the two composites have the ability to release Fe species, which further produced hydroxyl radicals (˙OH) to degrade pollutants.

It can be seen from the analysis of XPS full spectra of BC, FOC and FSC before reaction (Fig. 5 (a)), the photoelectron line at 281.9 and 533.2eV of BC, FOC and FSC corresponding to C 1s and O 1s, respectively. Furthermore, the photoelectron line at 708.8eV (Fe 2p) appeared in the XPS measurement spectra of FOC and FSC, S 2p (161.09eV) appeared in the measurement spectrum of FSC. The presence of Fe and S, which was consistent with the EDS and XRD analysis results, indicated that the preparation of FSC was successful, which could explain that with the addition of the element of S, it was probably that FSC might produce S intermediates and further promoted the degradation of NOR.

The magnetic property of the materials facilitated its separation and collection for reuse. The magnetic property of FOC and FSC were obtained via VSM, and the magnetization curve was shown in Figure S3. These two hysteresis loops indicated the magnetic strength of the two composites. The maximal magnetization saturation value of FOC and FSC were about 14.05 and 11.46 emu/g respectively, which were strong enough to separate from aqueous phase. The excellent magnetic properties of FOC and FSC indicated that these two materials could be practical applications and beneficial to magnetic separation in water pollution remediation.

Table 1
Basic physico-chemical properties of BC, FOC, FSC.

Samples	Yield (%)	BET Specific surface area (m^2/g)	Total pore volume(cm^3/g)	Average pore width (nm)	Elemental compositions (weight %)							
					C	O	Si	Mg	Al	Ca	Fe	S
BC	33.32	159.86	0.0882	2.21	33.19	38.46	27.93	–	–	–	–	–
FOC	42.40	134.96	0.0857	2.54	68.58	22.45	2.67	0.15	0.35	0.70	4.66	0.44
FSC	45.13	54.53	0.0532	3.90	56.41	26.31	5.72	0.10	0.19	0.03	4.58	6.65
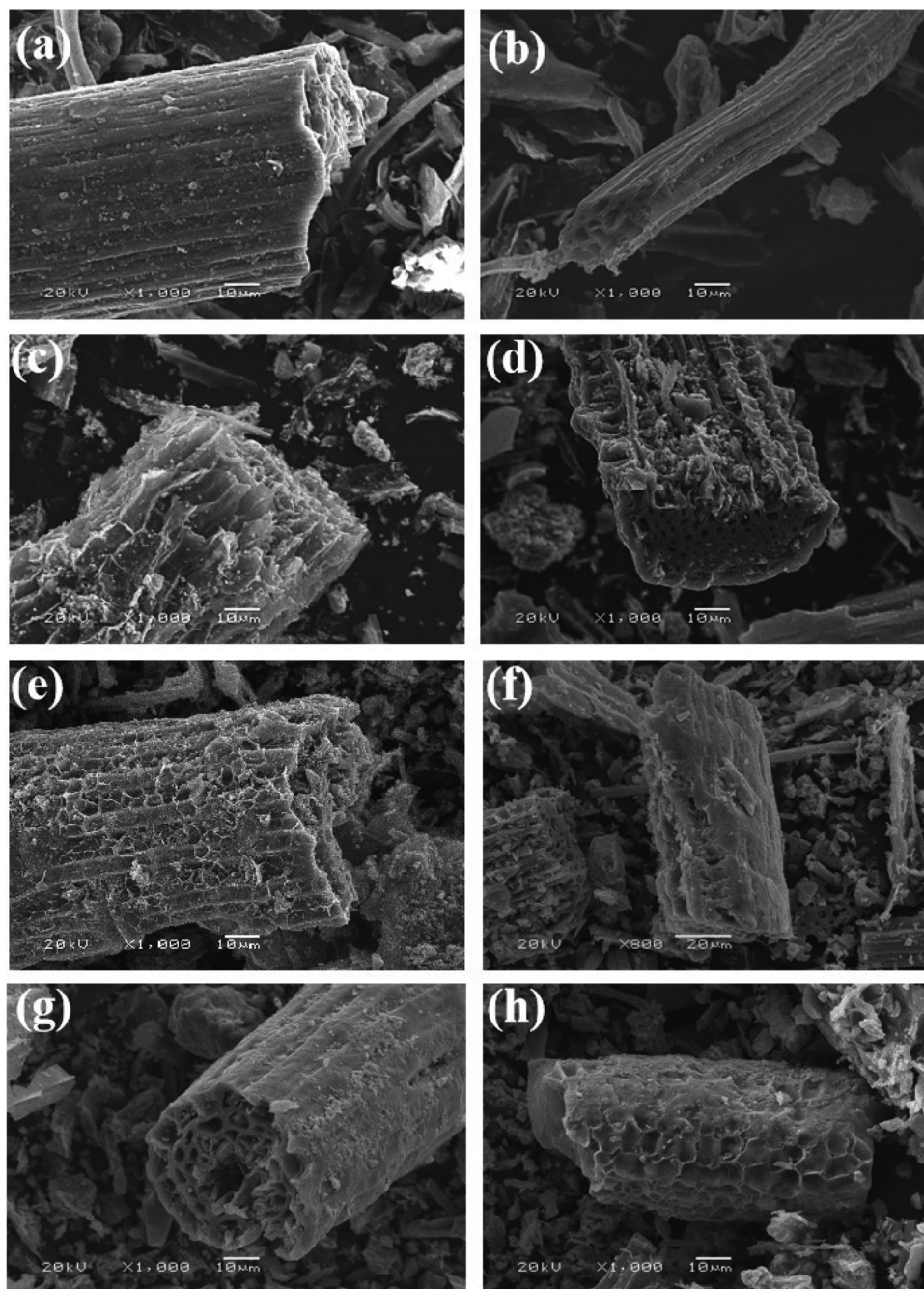
Fig. 1. SEM images of materials: (a) and (b) BC; (c) and (d) FOC and FSC before reaction; (e) and (f) FOC and FSC after reaction; (g) and (h) FOC and FSC after cycling.

4.2. Removal studies

4.2.1. Removal kinetics

The influence of reaction time on removal process of FOC and FSC were shown in Figure S4. In the initial phase, the removal capacity of NOR increased rapidly, and then increased slowly until reached the removal equilibrium after roughly 6 h. The fast removal phase might be ascribed to the availability of average pore width and a part of vacant active sites on the surface and the internal of FOC and FSC, and the slow increased stages might be ascribed to the gradual reduction of the efficient surface and internal active sites and the blocked pores with the increasing reaction time. Compared with the removal rate of BC (73.70%), FOC and FSC showed better removal capacity for NOR with 81.63% and 96.34% respectively. In particular, FSC had shown the best

removal capacity, which were about 1.11 and 1.31 times higher than that of FOC and BC. From what has been discussed above, FSC was proved to be an effective material for removing NOR compared with FOC and BC.

The experimental datas were simulated via using the pseudo-first-order kinetic, pseudo-second-order kinetic and intraparticle diffusion model to investigate removal mechanism of different time periods, which could be displayed as follows:

The pseudo-first-order kinetic model:

$$\lg(Q_e - Q_t) = \lg Q_e - \frac{k_1 t}{2.303} \tag{3}$$
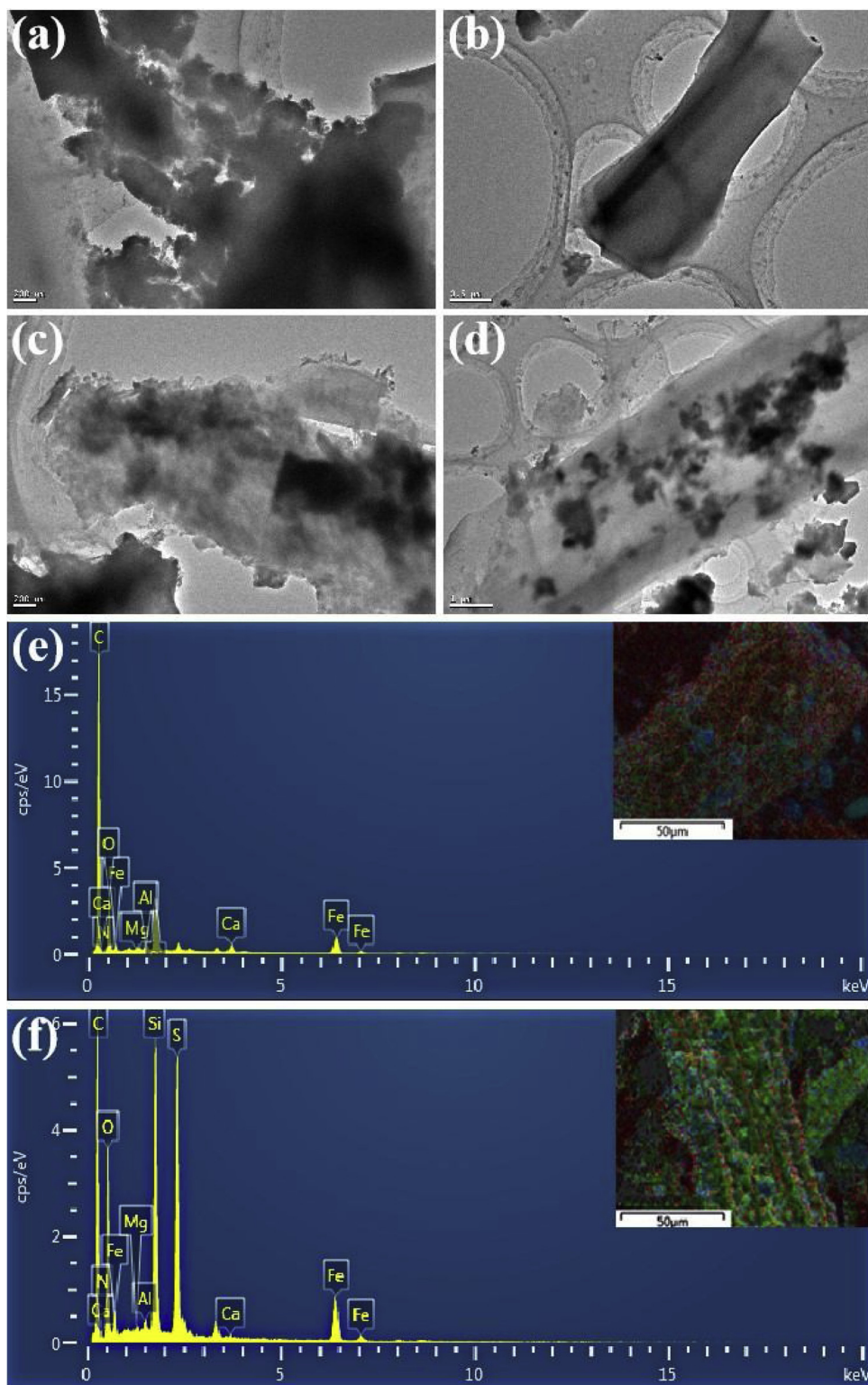
The pseudo-second-order kinetic model:

Fig. 2. TEM image: (a) and (b) FOC; (c) and (d) FSC and EDS spectrum graphs of (e) FOC and (f) FSC.

$$\frac{t}{Q_t} = \frac{1}{k_2 Q_e^2} + \frac{t}{Q_e} \tag{4}$$

The intraparticle diffusion model:

$$Q_t = K_{bi} t^{0.5} + C_i \tag{5}$$

where Q_e and Q_t (mg/g) are the equilibrium and time t (min) removal capacity of NOR respectively; k_1 (1/min), k_2 (g/(mg min)) and K_{bi} (mg/

(g min$^{0.5}$)) are the rate constants of the pseudo-first order, pseudo-second order and intraparticle diffusion model, respectively; C_i is the intercept corresponding to the boundary layer of stage i.

The kinetic model parameters for the removal of NOR by FOC and FSC were depicted in Table 2 and fitted curve were shown in Fig. 6. The results indicated that the pseudo-second-order model fitted the removal data on FOC and FSC better with the correlation coefficients (R^2) of 0.9990 and 0.9995, respectively. And it was also notable that the
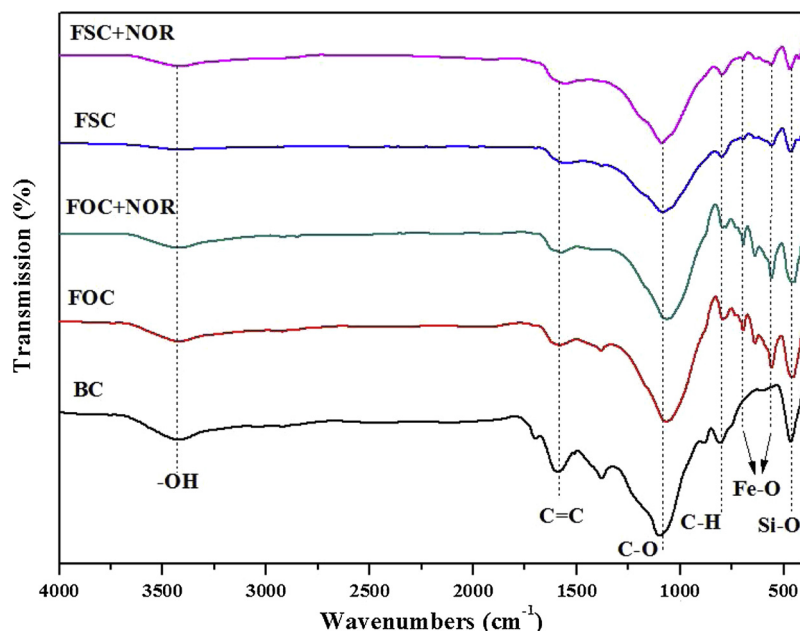
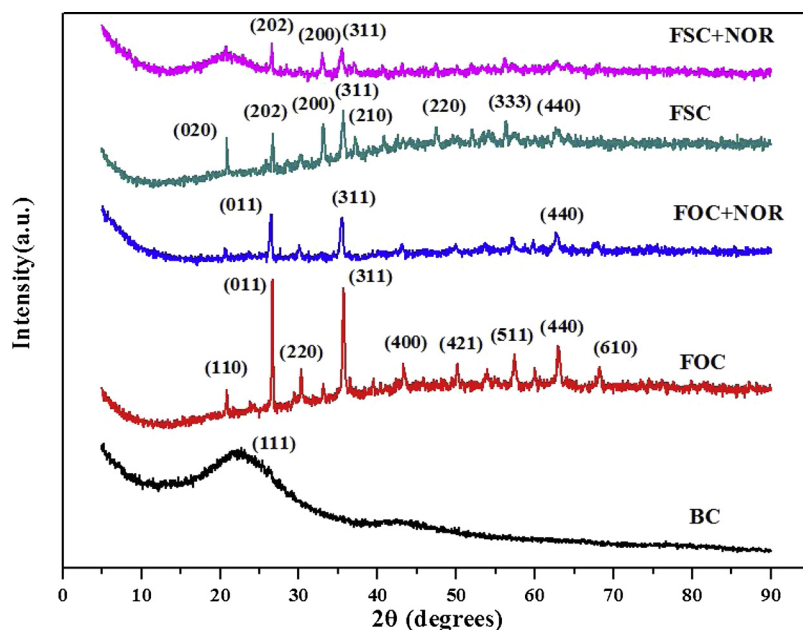**Fig. 3.** FTIR spectra of BC, FOC and FSC before and after reaction.

Fig. 4. XRD spectra of BC, FOC and FSC before and after reaction.

calculated values ($Q_{e,theo}$) from the pseudo-second-order model were much closer to the experimental values ($Q_{e,exp}$). These results revealed that the adsorption of NOR by FOC and FSC were chemisorption, which were involved the rate-limiting mechanism [49]. Therefore, the intraparticle diffusion model was used to determine the velocity limiting step the adsorption process. As depicted in Fig. 6 (c), the curve was not linear in the whole reaction time range and missed the origin, indicating that the adsorption of NOR by FOC and FSC carried out via three or more steps. The K_{bi} value, which represented the adsorption rate constants, was decreased from stage 1 to stage 3, indicating that the rate of adsorption was initially fast and slow down gradually. In addition, the Ci value, which represented the thickness of the boundary layers, was gradually increased. Based on the above results, both intraparticle diffusion and surface adsorption affected the actual adsorption process of FOC and FSC to NOR [50].

4.2.2. Removal isotherm and thermodynamic studies

Two widely used isotherm models (i.e. Langmuir and Freundlich) were used to fit experiment datas. The Langmuir model described the single-layer adsorption of the target compound on a homogenous surface, while the Freundlich model explained a multi-layer adsorption process [51]. In this study, removal isotherm of NOR by FOC and FSC for three different temperatures were depicted in Fig. 7, and the calculated adsorption constants were summarized in Table 3.

Langmuir isotherm:

$$Q_e = \frac{Q_m C_e K_L}{1 + C_e K_L} \tag{6}$$

$$R_L = \frac{1}{(1 + K_L C_0)} \tag{7}$$
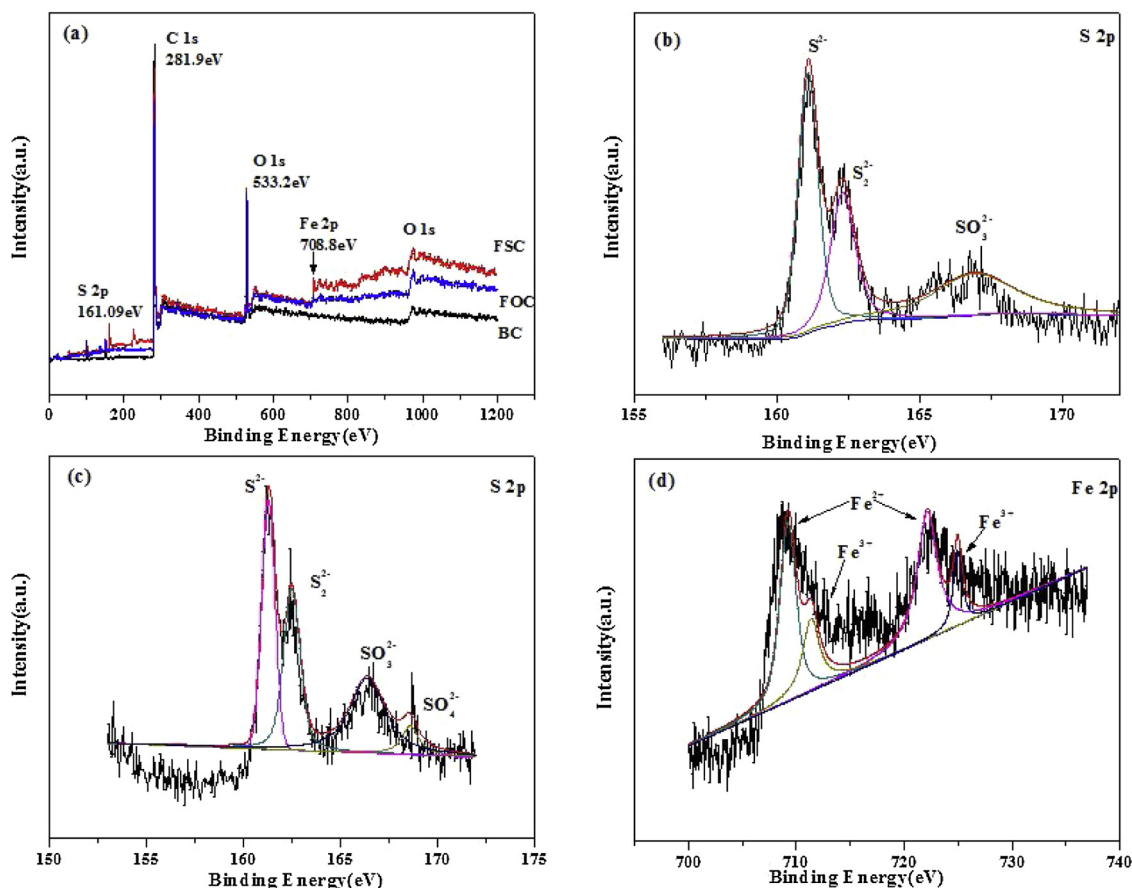
Freundlich isotherm:

Fig. 5. (a)XPS spectra of BC, FOC and FSC; (b) S 2p of FSC before reaction; (c) S 2p of FSC after reaction; (d) Fe 2p of FSC after reaction.

$$Q_e = K_f C_e^{\frac{1}{n}} \tag{8}$$

where Q_e (mg/g) and Q_m (mg/g) are the equilibrium amount of NOR absorbed onto the materials and the calculated maximum adsorption capacity respectively, C_e (mg/L) is the equilibrium concentration of NOR solution after reaction, K_f (mg$^{(1-n)}$ L^n/g^{-1}) and K_L (L/mg) represents the Freundlich affinity coefficient and the Langmuir bonding term related to interaction energies, respectively, n is the Freundlich linearityindex.

It was observed from Table 3 and Fig. 7 that the removal performance of NOR by FOC and FSC could be better described by the Freundlich isotherm model based on the higher correlation coefficients (R^2) compared with the Langmuir isotherm model. This indicated that the whole removal process of FOC and FSC to NOR was mainly multi-layer chemical adsorption. Additionally, K_f and n values represented the adsorption capacity and strength respectively. The results showed that at the 308k, both K_f and n values of FOC are higher than that of 288k, indicating that the adsorption were endothermic natures to NOR. However, the results of K_f and n values of FSC did not conform to the

above change rules, which explained the chaotic isotherm of FSC in Fig. 7 (b), and indicated that FSC had higher thermal stability. Furthermore, the calculated n values of FOC and FSC were higher than 1, which turned out that the adsorption of NOR molecules by FOC and FSC were favorable [52].

A comparison of the effect of different temperature (288 K, 298 K, and 308 K) towards the removal of NOR by FOC and FSC is significant and it always be calculated from three different temperature-dependent adsorption isotherms [53]. The thermodynamic parameters, such as the Gibbs free energy (ΔG^o, kJ/mol), standard enthalpy change (ΔH^o, kJ/mol), and standard entropy change (ΔS^o, kJ/(mol·K)), could be calculated by the following equations:

$$\Delta G^0 = -RT \ln K^t \tag{9}$$

$$\ln K^t = -\frac{\Delta H^0}{RT} + \frac{\Delta S^0}{R} \tag{10}$$

where T (K) is temperature, R (8.314 J/mol K) is the universal gas constant, and K^t is the adsorption equilibrium constants, obtained from

Table 2
Pseudo-first-order, pseudo-second-order and intraparticle diffusion model parameters for the removal of NOR by FOC and FSC.

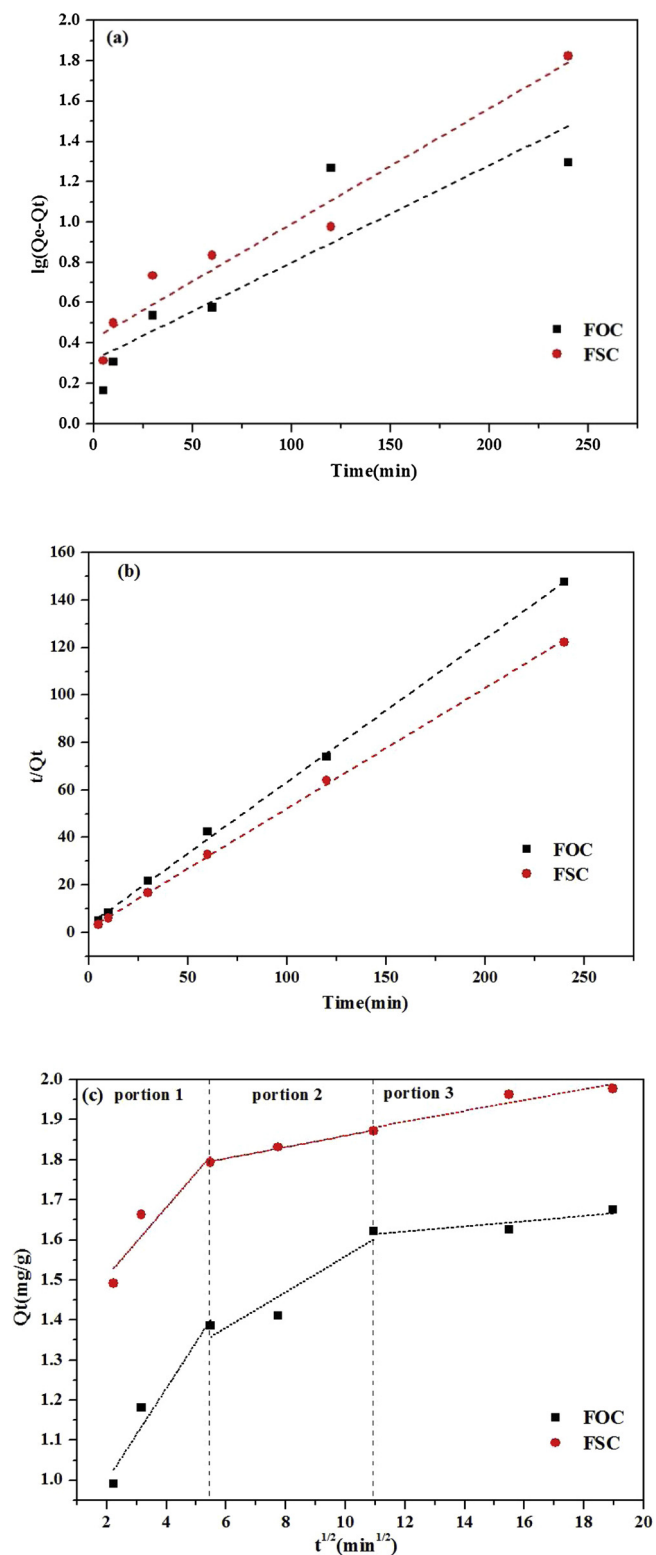| Composite materials	$Q_{e,exp}$(mg/g)	pseudo-first-order kinetic			pseudo-second-order kinetic			Intraparticle diffusion		
		$Q_{e,theo}$(mg/g)	k_1(min^{-1})	R^2	$Q_{e,theo}$(mg/g)	k_2(g/(mg min)	R^2	K_b [mg/(g·min$^{0.5}$)]	C	R^2
FOC	1.676	2.073	0.0111	0.8176	1.661	0.1099	0.9990	0.1152	0.7686	0.9506
								0.0446	1.1113	0.8969
								0.0065	1.5433	0.7323
FSC	1.978	2.636	0.0132	0.9548	1.973	0.2251	0.9995	0.0863	1.3364	0.9018
								0.0142	1.7181	0.9937
								0.0135	1.7327	0.9032

Fig. 6. Kinetic plot of the removal of NOR by FOC and FSC: (a) Pseudo-first-order; (b) Pseudo-second-order; (c) Intraparticle diffusion.

the linear plots of $\ln(1000 K^0)$ ($K^0(\text{L·g}^{-1}) = Q_e/C_e$; 1000 is the water density (g·L^{-1})) [54,55] versus C_e and extrapolating C_e to zero. The calculated values of these thermodynamic adsorption parameters were summarized in Table 4. In the present work, the results showed that the negative values of $\triangle G^0$ of FOC and FSC, indicating that the adsorption of NOR by FOC and FSC were spontaneous. However, the values of

$\triangle G^0$ of FOC became more negative with the increase of temperature, and the trend of $\triangle G^0$ of FSC was the opposite. It signified the fact that the adsorption process of FOC was more thermodynamically feasible than that of FSC [56], and it also revealed that FSC had higher thermal stability, which was consistent with the adsorption isotherm results. The positive values of $\triangle H^0$ of FOC further confirmed the endothermic nature in the adsorption process of NOR, while FSC exhibited exothermic nature because of the negative values of $\triangle H^0$. Moreover, the positive values of $\triangle S^0$ of FOC revealed that the degree of freedom of NOR molecules adsorbed at the solid-solution interface on the binding site of the materials decreased, representing a strong binding of NOR molecule onto the active sites, and the negative values of $\triangle S^0$ indicated a decrease in the degree of freedom during the adsorption of NOR by FSC [57]. This might be attributed to the fact that when NOR molecules adsorbed on the surface of the materials, the surface movement was limited and the disorder degree decreased [58].

4.3. Effect of pH on NOR removal

The pH value of solution is considered to be the major factor affecting the removal of NOR by materials by changing both the form of the target pollutants and the surface binding sites of the materials [59]. On account of that it affected both the pH of zero point charges (pH$_{pzc}$) of the materials and the molecular form of NOR in solution. In order to investigate the effects of initial solution pH on NOR removal, batch experiments were conducted at different pH from 2.0 to 11.0 and the pH of zero point charges (pH$_{pzc}$) of the two materials were also measured. Learning from Fig. 8, the pH$_{pzc}$ of FOC and FSC exhibited about 7.72 and 4.02, and the materials surface were negatively charged at pH values greater than pH$_{pzc}$, on the contrary, it was positively charged [51]. In addition, there are two proton binding sites (carboxyl and piperazinyl group) of NOR with pKa values of 6.22 and 8.51, respectively. Thus, at different pH levels, NOR could exist in the corresponding ions, such as cationic form (NOR$^+$), zwitterionic and neutral form (NOR$^\pm$/NOR^0), or anionic form (NOR$^-$) [60].

As it exhibited in Fig. 8, the removal rate of FOC and FSC to NOR presented a rising trend with the pH range of 2.0-4.0. At a lower pH, the lower removal of NOR on the materials was mainly ascribed to the competitive effect between H$^+$ and NOR$^+$, and as the initial pH of the solution increased, the equilibrium pH also gradually increased, leading to a gradual increase in the removal. The maximum NOR adsorption capacity of FOC was 2.45 mg/g with the pH of 4.0, whereas that of FSC was steady in the initial pH of 4.0-11.0. And then there was a descending trend for FOC with pH of 4.0–5.0, and a fluctuation within a narrow range with a wide pH range of 5.0–11.0. These probably due to the fact that as the initial pH of the solution gradually reached the median of pKa$_1$ and pKa$_2$ or above pKa$_2$, zwitterionic (NOR$^\pm$/NOR^0) and anionic form (NOR$^-$) grew and lead to a minor change in the removal. In addition, the pH of the equilibrium solution was changed in a noticeable range from 1.91 to 8.22 for FOC in the stage of the initial pH from 2.0 to 4.0 and then steadied at 8.57 in the pH range of 4.0-11.0. Correspondingly, the pH of the equilibrium solution of FSC presented the same changing trend and steadying at 5.35 to 5.60 ultimately. It could be inferred that the stability of removal with the pH of 5.0–11.0 was mainly due to the buffering effect of the materials itself. The above experimental results indicated that, the electrostatic effects between the two materials and NOR were not significant in the stage of initial pH from 5.0 to 11.0 because of the strong buffering capacities.

4.4. The effect of Ionic strength on NOR removal

In order to explore the removal effect of NOR from aqueous solution with the two materials under different ionic strength conditions, Ca^{2+} was selected in the experiment with three different ionic strengths (0.001, 0.01 and 0.1 mol/L). As Figure S5 can been seen, under the same ionic strength, as the initial concentration of the solution
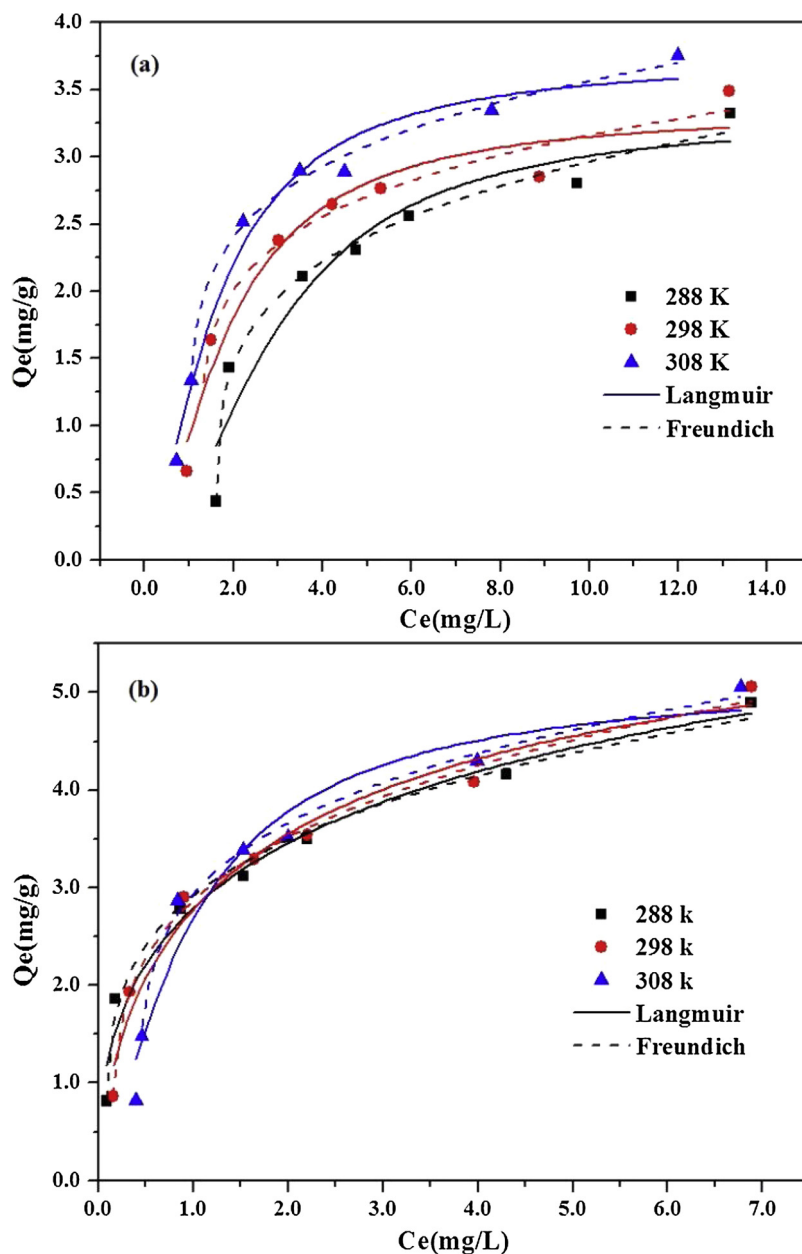
Fig. 7. Removal isotherm of NOR by materials at different temperatures (a) FOC; (b) FSC.

increased, the removal of NOR by the two materials increased gradually until the removal equilibrium was reached. As the ionic strength increased, the removal of NOR by FOC (Figure S5 (a)) in aqueous solution was significantly reduced. It indicated that the higher concentration of Ca^{2+}, the greater influence of FOC on the adsorption of NOR molecules

and it could be due to the competitive adsorption between Ca^{2+} and NOR^+ in adsorption process, which inhibits the effective contact between NOR and the surface of FOC, and the effect of ion competition on NOR removal was demonstrated [61]. Conversely, the ionic strength in the solution had little effect on FSC and it was almost negligible (Figure

Table 3
Langmuir and Freundlich isotherm parameters under different temperatures for the removal of NOR by FOC and FSC.

Composite materials	The temperature(K)	Langmuir isotherm			Freumdlich isotherm		
		R^2	K_L (L/mg)	Q_m (mg/g)	R^2	K_f [mg/g)·(1/mg)$^{1/n}$]	1/n
FOC	288.15	0.8714	0.1872	4.6522	0.9883	1.8162	0.2300
	298.15	0.9166	0.3815	4.0740	0.9307	2.1188	0.1846
	308.15	0.9527	0.4436	4.4699	0.9879	2.4035	0.1796
FSC	288.15	0.8936	2.0526	4.6454	0.9872	2.9836	0.2410
	298.15	0.9456	1.1311	5.1056	0.9913	2.9992	0.2591
	308.15	0.9359	0.7734	5.9425	0.9874	3.3243	0.2163

Table 4
Thermodynamic adsorption parameters.

	T(K)	lnK (L/mg)	ΔG^O (KJ/mol)	ΔH^O (KJ/mol)	ΔS^O [KJ/(mol·K)]
FOC	288.15	5.3991	−12.9345	49.2746	0.2168
	298.15	6.3541	−15.7507		
	308.15	6.7294	−17.2404		
FSC	288.15	8.5753	−20.5437	−31.9914	−0.0396
	298.15	8.2069	−20.3434		
	308.15	7.7059	−19.7422		
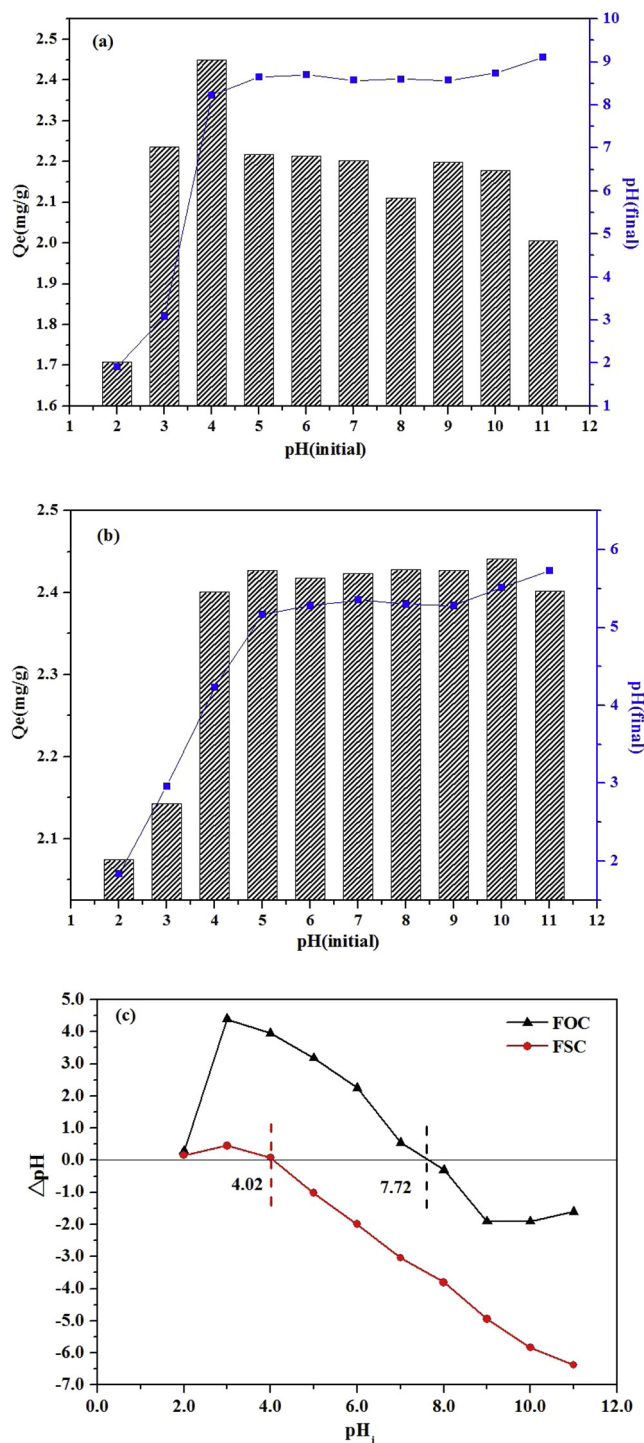
Fig. 8. Effects of initial solution pH on the removal of NOR: (a) FOC, (b) FSC and (c) the pH$_{pzc}$ of FOC and FSC.

S5 (b)). It was shown that FSC had excellent adsorption capacity, which was mainly due to the excellent structures and properties of FSC itself and the differences between the types of iron mineral materials attached to the surface.

4.5. Regeneration study

Considering the feasibility and practical application of two composites (FOC and FSC), it was extremely important to explore the repeated regeneration performance and stability of materials. After preliminary experimentation, it was decided to select methanol and deionized (DI) water as the cleaning solution for this experiment. After each removal of NOR, the separated materials were washed five times and drying at 80℃ under anaerobic conditions to the next experiments and repeated 5 times. The results were shown in the Figure S6. The removal capacity of the two materials for NOR decreased slightly after the first cycle experiment and then the removal rate of NOR by FOC and FSC fluctuated slightly, and eventually stabilized at around 75% and 83% respectively. This indicated that after several cycles, the removal rate of NOR decreased only after the first time, and then maintained stable and excellent adsorption performance. This might be mainly due to the structural properties of the two composites themselves. In addition, the recovery rate of FOC and FSC after each cyclic experiment was about 90%. In summary, both the two materials had strong regeneration ability and were easy to recycle, which indicated that they had good application values in the actual treatment of pollution.

4.6. The removal mechanism and degradation pathway of NOR

Based on the SEM images of FOC and FSC after reaction (Fig. 1(e) and (f)) and after cycling (Fig. 1(g) and (h)), it is observed that there are obvious flocculated pollutant particles attached to the surface of these two materials after the reaction, which make the surface more homogeneous and the pore channels are filled. After multiple cycles, there are no significant changes in these structural features of FOC and FSC compared with that after the first reaction. In view of the FTIR spectra of FOC and FSC after reaction (Fig. 3), these peaks (e.g. 3426, 1588, 1099, 807 and 465 cm^{-1}, corresponding to −OH, C=C, C−O, C−H and Si−O) all had a slight red shift, and it could be speculated that these groups may be involved in the NOR removal reaction. The shift and decrease of C=C, C−O and C−C indicated that the significant role of π–π interactions between NOR and FOC and FSC in the reaction process [42]. The weakening of −OH indicated that hydrogen-bonding interactions were important. Meanwhile, the band of Fe-O (695 and 561 cm^{-1}) and Si−O (456 cm^{-1}) also diminished slightly, which confirmed that the Fe−O or Si−O provided more adsorption sites for the removal of NOR. Additionally, the XRD spectrum after the reaction (Fig. 4) indicated that the corresponding characteristic peaks of these two materials decreased only slightly compared with that before the reaction, indicating that they had good stability, especially for FSC.

Sulfate radicals (SO$_4$·$^-$) are usually produced by activation of peroxymonosulfate (PMS, HSO$_5^-$) and persulfate (PS, S$_2$O$_8^{2-}$) [62]. Meanwhile, sulfate radicals (SO$_4$·$^-$) and hydroxyl radical (·OH) have been reported to generate from PMS activation by FeS$_2$ [33]. Due to the introduction of natural pyrite (FeS$_2$), it was speculated that ·OH and SO$_4$·$^-$ might be generated in the reaction process.

To ascertain the mechanism for the removal of NOR by FOC and FSC, effects of different amounts of radical scavengers on NOR degradation by FOC and FSC were determined in Fig. 9 (a) and it showed that the NOR removal efficiency of FOC decreased from 82% to 78% and 71% with the addition of 0.1 mg/L and 0.5 mg/L tert-butyl alcohol (TBA) respectively, while that of FSC decreased from 96% to 94% and 86% [63]. The results indicated that ·OH would be the dominant radical of NOR degradation, meanwhile it would be derived from the reaction between SO$_4$·$^-$ and H$_2$O (Eqs. (11)) [33]. While, SO$_4$·$^-$ might be generated in the reaction system of NOR/FSC and became the
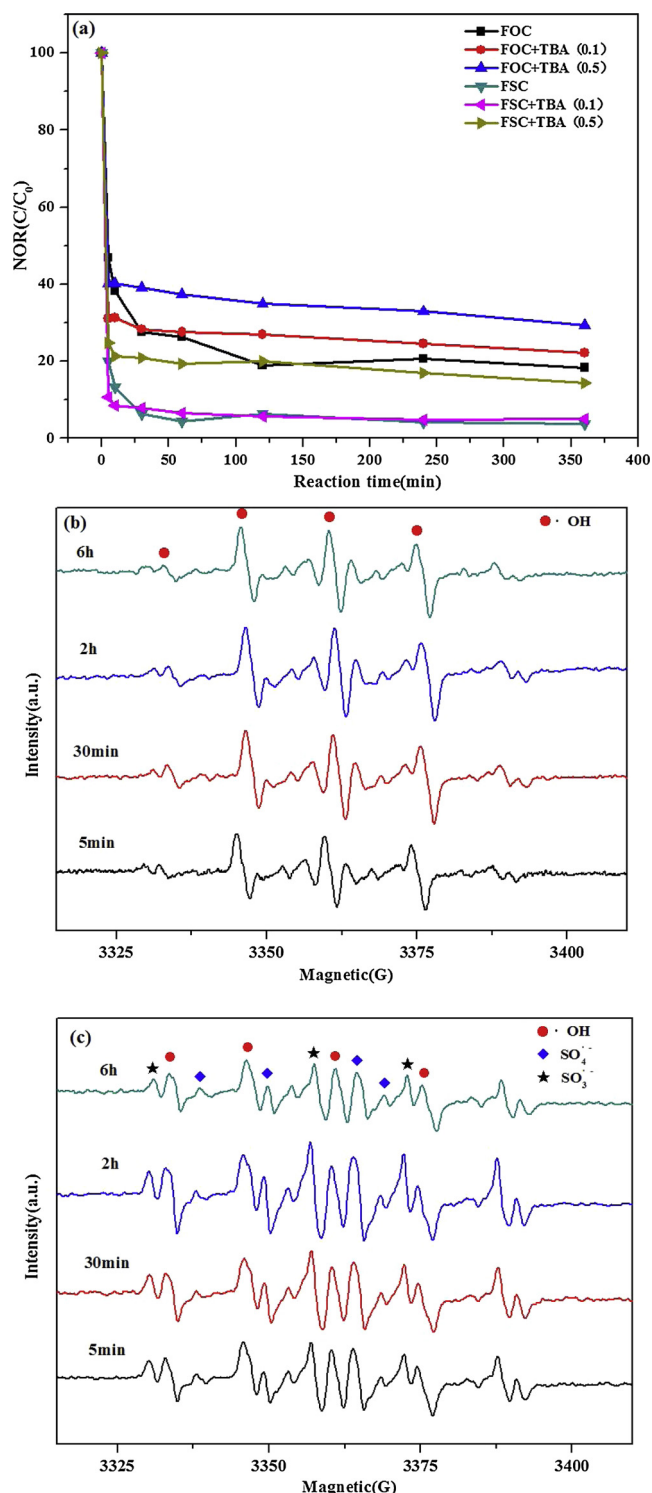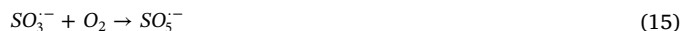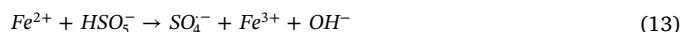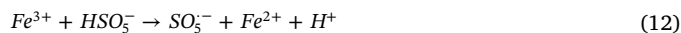
Fig. 9. (a) Removal efficiency of NOR under the conditions of different tert-butyl alcohol (TBA) concentration; EPR spectrum of free radicals generated in the (b) NOR/FOC system; (c) NOR/FSC system at different reaction times.

dominant radical for NOR removal. Here, to cast more light on the reaction mechanism, as the spin trap, 2.0 μL DMPO was used in EPR spectroscopy, which was applied for identifying the primary radicals in the two different reaction systems. DMPO was used to trap the generated free radicals, and the signals corresponding to the DMPO−OH, DMPO-SO$_4$ and DMPO-SO$_3$ adducts indicated the existence of ·OH, SO$_4$·$^-$ and SO$_3$·$^-$, respectively [64]. As presented in Fig. 9 (b), the typical DMPO−OH spin adduct possessed a characteristic 1:2:2:1

quadruple were observed in NOR/FOC reaction system [65]. Moreover, EPR signals for DMPO-SO$_3$, DMPO-SO$_4$ and DMPO−OH adducts were observed in Fig. 9 (c) and this demonstrated that SO$_3$·$^-$, SO$_4$·$^-$ and ·OH could be generated in NOR/FSC reaction process. Furthermore, extending the reaction time from 5 min to 2 h, the peak intensities of EPR signals increased gradually, with only slight falling from 2 h to 6 h, which indicated that the content of free radicals changed with reaction times [66], and it was consistent with the consequence of the removal kinetics.

Due to the introduction of natural pyrite, FSC would oxidize to produce a sulfur-enriched surface and dissolved Fe species would be also released in the reaction solution [67], then some reduced sulfur intermediates such as S^{2-} and S$_2$O$_3$$^{2-}$ would be produced on the surface of FSC, meanwhile, disulfides (e.g. S$_2$$^{2-}$) and polysulphides would be oxidized by Fe (III) produced S species (SO$_3$$^{2-}$/SO$_4$$^{2-}$) [33], Fe (III) would be reduced to Fe (II) by S$_2$$^{2-}$ via one electron-transfer process and Fe (II) would also be generated by the oxidation of Fe (III) (Eqs (12)-(13)). Considering the electronegativity of biochar [68], this process may be facilitated. In addition, XPS was used to characterize FSC after reaction and Fig. 5 (c) and (d) displayed the presence of S$_2$$^{2-}$/S^{2-}/SO$_3$$^{2-}$/SO$_4$$^{2-}$ and Fe (II), Fe (III) [41], which were the dominant Fe and S species. Furthermore, the coexistence of SO$_3$$^{2-}$ and Fe (III) had been reported to initiate radical chain reactions to produce SO$_3$ and SO$_4$·$^-$ radicals based on the following reactions [69] (Eqs. (14)-(16)), which were consistent with EPR results.

$$SO_4^- + H_2O \rightarrow ·OH + H^+ \tag{11}$$

$$Fe^{3+} + HSO_5^- \rightarrow SO_5^{·-} + Fe^{2+} + H^+ \tag{12}$$

$$Fe^{2+} + HSO_5^- \rightarrow SO_4^{·-} + Fe^{3+} + OH^- \tag{13}$$

$$Fe^{3+} + SO_3^{2-} \rightarrow SO_3^{·-} + Fe^{2+} \tag{14}$$

$$SO_3^{·-} + O_2 \rightarrow SO_5^{·-} \tag{15}$$

$$SO_3^{2-} + SO_5^{·-} \rightarrow SO_4^{2-}SO_4^- \tag{16}$$

Due to the introduction of natural pyrite, additional sulfate radical would be produced in the reaction process compared with the introduction of natural hematite. EPR spectroscopy results confirmed that hydroxyl radical and sulfate radical existed in NOR/FSC reaction system, which might be the major reason why the removal performance of FSC was better than that of FOC. Meanwhile, Fe (II) would be generated via the reduction of Fe (III) by S$_2$$^{2-}$, and these were also the key steps controlling the production of free radicals and the degradation of NOR [33]. Combined with the above results, a possible mechanism of the removal of NOR by FOC and FSC was proposed as shown in Figure S7.

In the course of the reaction, the TOC content of the samples with different reaction times were determined. As depicted in Figure S8, with the increase of reaction times, the removal efficiency of TOC in different samples were basically unchanged, only remaining at around 10%, which indicated that in the process of reaction, the NOR molecular were all almost degraded to low molecular organic intermediates. Meanwhile, during the NOR degradation process, different intermediates and degradation products in the reaction of FOC and FSC were detected by HRMS in positive mode. Combined with the detection results, the NOR transformation pathways were established and shown in Fig. 10. In the reaction system of NOR/FOC (Fig. 10 (a)), including four major steps of ring opening, substitution of fluorine (F), decarboxylation and defluorination because of the production of ·OH. Intermediates A with a protonated form of m/z 279 was clearly detected in the HRMS spectrum, and it could react with ·OH to generate B (m/z = 204), and then generated C (m/z = 188) and D (m/z = 174) through dehydroxylation and decarbonylation [70]. After substitution of fluorine (F) with −OH [71,72], intermediates E (m/z = 318) could also react with ·OH to generate two intermediates, K (m/z = 334) and G (m/z = 257) [73].
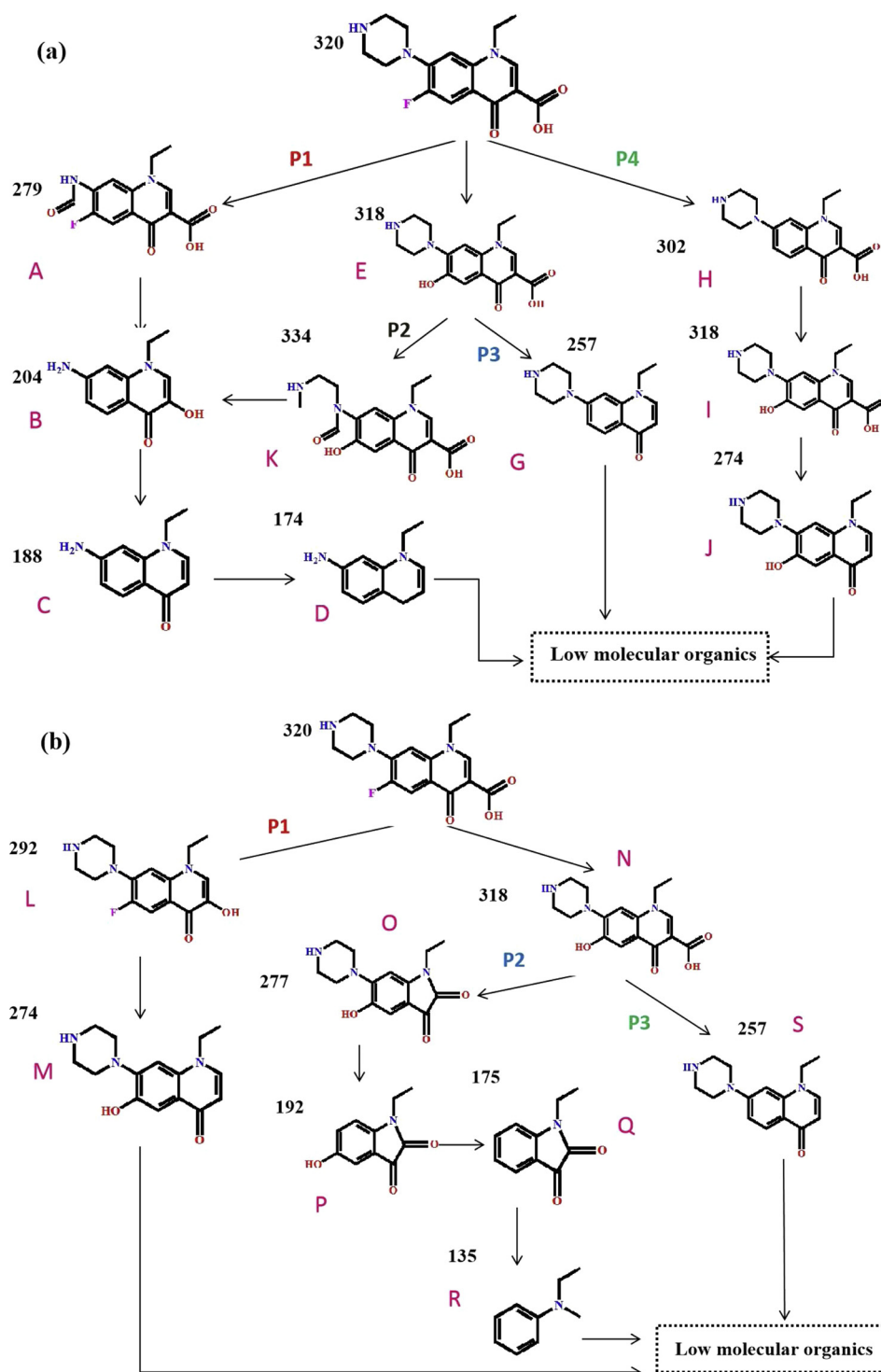
Fig. 10. Degradation pathways of NOR with the reaction of (a) FOC and (b) FSC.

And product K would generate B by further reactions. Additionally, in terms of pathway IV, intermediates H with protonated form at m/z 302, was probably produced due to the defluorination reaction. Then it was transferred to product I ($m/z = 318$) via hydroxylation reaction. Finally, the hydroxylated product I was transformed into product J ($m/z = 274$) through decarboxylation reaction [74]. As depicted in Fig. 10 (b), since ˙OH and SO_4˙⁻ that were produced attacked target contaminant through some reaction mechanisms, i.e., substitution of fluorine (F), dehydroxylation, decarbonylation, transformations of quinolone and piperazinyl groups simultaneously or successively

occurred in this case [71], there were three major pathways involved in the reaction system of NOR/FSC. Two possible intermediates at $m/z = 292$ and $m/z = 318$ would be formed firstly, which were remarked as intermediates L and N respectively. The intermediates L was formed by substitution reaction of −COOH group, and then product M was formed via the loss of oxygen and substitution of fluorine (F) [71]. In addition, intermediates N ($m/z = 318$) was formed by substitution of fluorine (F) subsequently, unsaturated bond would be attacked and yield intermediates O ($m/z = 277$) through the loss of −CO and −H-COOH [71]. Finally, product R ($m/z = 135$) was formed through a

series of reactions. Meanwhile, intermediates N could also yield product S (m/z = 257) by dehydroxylation and decarboxylate, which would be mineralized to low molecular organic intermediates through further oxidation finally.

5. Conclusion

In the present study, two novel magnetic iron ore biochar composites (FOC and FSC) were prepared successfully, and used for NOR removal in aqueous solution. Multiple characterization results revealed that after the introduction of natural hematite and natural pyrite, the average pore width increased obviously, especially for FSC, meanwhile, there were more functional groups in the surface of FOC and FSC, which could interact with NOR via hydrogen bonding, π-π electron acceptor donor action, complexation and ion exchange interaction. Effects of pH on NOR removal could be ignored with the pH range of 5.0–11.0 because of the buffering effect of the materials itselves. And the ionic strength (Ca^{2+}) in the solution had little effect on FSC. Furthermore, free radicals quenching combined with EPR results indicated that in the reaction system of NOR/FSC, FSC could produce $\cdot OH$ and $SO_4^{\cdot-}$, which were facilitated for NOR degradation. With the help of HRMS analysis, different degradation products in the two reaction systems were detected, which were significant for the theoretical study of NOR removal and degradation mechanism of pollutants by $\cdot OH$ and $SO_4^{\cdot-}$.

Acknowledgements

Appendix A. Supplementary data

Supplementary material related to this article can be found, in the online version, at doi:https://doi.org/10.1016/j.apcatb.2019.117752.

References

[1] C. Guo, S. Gao, J. Lv, S. Hou, Y. Zhang, J. Xu, Appl. Catal. B 205 (2017) 68–77.
[2] W. Liao, V.K. Sharma, S. Xu, Q. Li, L. Wang, Int. J. Environ. Res. Public Health 14 (2017) 1564–1681.
[3] G. Mamba, J. Kiwi, C. Pulgarin, R. Sanjines, S. Giannakis, S. Rtimi, Appl. Catal. B 233 (2018) 175–183.
[4] K. Kümmerer, A. Al-Ahmad, V. Mersch-Sundermann, Chemosphere 40 (2000) 701–710.
[5] N. Millar, S. Siebert, I. McInnes, Nature (2019), https://doi.org/10.1038/d41586-019-00619-7.
[6] M. Feng, L. Cizmas, Z. Wang, V.K. Sharma, Chemosphere 177 (2017) 144–148.
[7] H. LI, J. Chen, H. Hou, H. Pan, X. Ma, J. Yang, L. Wang, J.C. Crittenden, Water Res. 126 (2017) 274–284.
[8] S. Mosleh, M.R. Rahimi, M. Ghaedi, K. Dashtian, S. Hajati, RSC Adv. (2016), https://doi.org/10.1039/C6RA10385E.
[9] S. Mosleh, M.R. Rahimi, M. Ghaedi, K. Dashtian, S. Hajati, S. Wang, Chem. Eng. Process. 114 (2017) 24–38.
[10] S. Jalali, M.R. Rahimi, K. Dashtian, M. Ghaedi, S. Mosleh, Polyhedron 166 (2019) 217–225.
[11] S. Mosleh, M.R. Rahimi, M. Ghaedi, K. Dashtian, S. Hajati, RSC Adv. 6 (2016) 17204.
[12] M. Amiri, K. Dashtian, M. Ghaedi, S. Mosleh, R. Jannesar, New J. Chem. 43 (2019) 1275.
[13] S. E. Mousavinia, S. Hajati, M. Ghaedi, K. Dashtian, 2016, DOI: 10.1039/c6cp00910g.
[14] K. Dashtian, M. Ghaedi, H. Shirinzadeh, S. Hajati, S. Shahbazi, Chem. Eng. J. 339 (2018) 189–203.
[15] X. Zhou, J. Zhou, Y. Liu, J. Guo, J. Ren, F. Zhou, Fuel 233 (2018) 469–479.
[16] D. Shan, S. Deng, T. Zhao, B. Wang, Y. Wang, J. Huang, G. Yu, J. Winglee, M.R. Wiesner, J. Hazard. Mater. 305 (2016) 156–163.
[17] H. Liu, F. Xu, Y. Xie, C. Wang, A. Zhang, L. Li, H. Xu, Sci. Total Environ. 645 (2018) 702–709.
[18] X. Jing, Y. Wang, W. Liu, Y. Wang, H. Jiang, Chem. Eng. J. 248 (2014) 168–174.
[19] H. Wang, C. Fang, Q. Wang, Y. Chu, Y. Song, Y. Chen, X. Xue, RSC Adv. 8 (2018) 16260–16268.
[20] X. Zhu, C. Li, J. Li, B. Xie, J. Lü, Y. Li, Bioresour. Technol. 263 (2018) 475–482.
[21] K. Sun, K. Ro, M. Guo, J. Novak, H. Mashayekhi, B. Xing, Bioresour. Technol. 102 (2011) 5757–5763.
[22] Y. Qiu, Z. Zhang, Z. Zhou, G.D. Sheng, Bioresour. Technol. 100 (2009) 5348–5351.
[23] T. Zhao, Y. Yao, D. Li, F. Wu, C. Zhang, B. Gao, Sci. Total Environ. 640–641 (2018) 73–79.
[24] Y. Yao, B. Gao, J. Chen, Y. Yang, Environ. Sci. Technol. 47 (2013) 8700–8708.
[25] M.B. Ahmed, J.L. Zhou, H.H. Ngo, W. Guo, M. Chen, Bioresour. Technol. 214 (2016) 836–851.
[26] P. Liu, W. Liu, H. Jiang, J. Chen, W. Li, H. Yu, Bioresour. Technol. 121 (2012) 235–240.
[27] F. Reguyal, A. Sarmah, Sci. Total Environ. 628–629 (2018) 722–730.
[28] Y. Zhou, X. Liu, Y. Xiang, P. Wang, J. Zhang, F. Zhang, J. Wei, L. Luo, M. Lei, L. Tang, Bioresour. Technol. 245 (2017) 266–273.
[29] Y. Li, Y. Zhang, G. Wang, S. Li, R. Han, W. Wei, J. Mol. Liq. 263 (2018) 53–63.
[30] H. Zhao, Y. Lang, J. Taiwan Inst. Chem. Eng. 88 (2018) 152–160.
[31] T. Suzuki, T. Yano, M. Hara, T. Ebisuzaki, Appl. Surf. Sci. 674 (2018) 6–12.
[32] Y. Lü, Z. Li, J. Li, K. Chen, H. Dong, J. Shou, Y. Li, Chem. Eng. J. 349 (2018) 522–529.
[33] Y. Zhou, X. Wang, C. Zhu, D.D. Dionysiou, G. Zhao, G. Fang, D. Zhou, Water Res. 142 (2018) 208–216.
[34] J. Yuan, R. Xu, H. Zhang, Bioresour. Technol. 102 (2011) 3488–3497.
[35] Y. Li, Z. Wang, X. Xie, J. Zhu, R. Li, T. Qin, Colloids Surf. A: Physicochem. Eng. Aspects 514 (2017) 126–136.
[36] S.A.C. Carabineiro, T. Thavorn-Amornsri, M.F.R. Pereira, J.L. Figueiredo, Water Res. 4 (45) (2011) 4583–4591.
[37] X. Peng, X. Hu, D. Fu, F.L.Y. Lam, Appl. Surf. Sci. 294 (2014) 71–80.
[38] B. Chen, Z. Chen, S. Lv, Bioresour. Technol. 102 (2011) 716–723.
[39] L. Lian, X. Cao, Y. Wu, D. Sun, D. Lou, Appl. Surf. Sci. 289 (2014) 245–251.
[40] H. Mao, S. Wang, J. Lin, Z. Wang, J. Ren, J. Environ. Sci. 49 (2016) 179–188.
[41] S. Zhang, H. Gao, J. Huang, X. Wang, T. Hayat, J. Li, X. Xu, X. Wang, Environ. Sci. Nano 5 (2018) 1179–1190.
[42] J. Tang, Y. Huang, Y. Gong, H. Lyu, Q. Wang, J. Ma, J. Hazard. Mater. 316 (2016) 151–158.
[43] M. Brigante, E. Pecini, M. Avena, Microporous Mesoporous Mater. 230 (2016) 1–10.
[44] J. Wang, Z. Chen, B. Chen, Environ. Sci. Technol. 48 (2014) 4817–4825.
[45] X. Guo, C. Yang, Y. Wu, Z. Dang, Environ Sci Pollut Res. 21 (2014) 2572–2580.
[46] M. Zhang, B. Gao, S. Varnoosfaderani, A. Hebard, Y. Yao, M. Inyang, Bioresour. Technol. 130 (2013) 457–462.
[47] R. Vijayakumar, Y. Koltypin, I. Felner, A. Gedanken, Mater. Sci. Eng. A 286 (2000) 101–105.
[48] H. Lyu, J. Tang, Y. Huang, L. Gai, E.Y. Zeng, K. Liber, Y. Gong, Chem. Eng. J. 322 (2017) 516–524.
[49] M. Li, Q. Liu, L. Guo, Y. Zhang, Z. Lou, Y. Wang, G. Qian, Bioresour. Technol. 141 (2013) 83–88.
[50] H. Li, D. Zhang, X. Han, B. Xing, Chemosphere 95 (2014) 150–155.
[51] A.A. Bazrafshan, S. Hajati, M. Ghaedi, RSC Adv. 5 (2015) 79119–79128.
[52] F. Yu, J. Chen, L. Chen, J. Huai, W. Gong, Z. Yuan, J. Wang, J. Ma, J. Colloid Interface Sci. 378 (2012) 175–183.
[53] C. Luo, Z. Tian, B. Yang, L. Zhang, S. Yan, Chem. Eng. J. 234 (2013) 256–265.
[54] S.K. MILONJIĆ, J. Serb. Chem. Soc. 72 (12) (2007) 1363–1367.
[55] T.R.S. Cadaval Jr, G.L. Dotto, L.A.A. Pinto, Chem. Eng. Commun. (2019), https://doi.org/10.1080/00986445.2014.934449.
[56] Y. Li, Z. Di, J. Ding, D. Wu, Z. Luan, Y. Zhu, Water Res. 39 (2005) 605–609.
[57] W. Konicki, K. Cendrowski, X. Chen, E. Mijowska, Chem. Eng. J. 228 (2013) 824–833.
[58] M.J. Iqbal, M.N. Ashiq, J. Hazard. Mater. B 139 (2007) 57–66.
[59] G. Wu, J. Ma, S. Li, J. Guan, B. Jiang, L. Wang, J. Li, X. Wang, L. Chen, J. Colloid Interface Sci. 528 (2018) 360–371.
[60] W. Yang, Y. Lu, F. Zheng, X. Xue, N. Li, D. Liu, Chem. Eng. J. 179 (2012) 112–118.
[61] Z. Li, L. Schulz, C. Ackley, N. Fenske, J. Colloid Interface Sci. 351 (2010) 254–260.
[62] S. Zhang, S. Song, P. Gu, R. Ma, D. Wei, G. Zhao, T. Wen, R. Jehan, B. Hu, X. Wang, J. Mater. Chem. A Mater. Energy Sustain. 7 (2019) 5552–5560.
[63] S. Zhang, Y. Liu, P. Gu, R. Ma, T. Wen, G. Zhao, L. Li, Y. Ai, C. Hu, X. Wang, Appl. Catal. B 248 (2019) 1–10.
[64] J. Zou, J. Ma, L. Chen, X. Li, Y. Guan, P. Xie, C. Pan, Environ. Sci. Technol. 47 (2013) 11685–11691.
[65] H. Gao, R. Cao, X. Xu, S. Zhang, Y. Huang, H. Yang, X. Deng, J. Li, Appl. Catal. B: Environ. (2019), https://doi.org/10.1016/j.apcatb.2019.01.004.
[66] J. Fan, L. Gu, D. Wu, Z. Liu, Chem. Eng. J. 333 (2018) 657–664.
[67] J.D. Rimstidt, D.J. Vaughan, Geochim. Cosmochim. Acta 5 (2003) 873–880.
[68] S. Li, Z. Wang, X. Zhao, X. Yang, G. Liang, X. Xie, Chem. Eng. J. 360 (2019) 600–611.
[69] L. Chen, M. Tang, C. Chen, M. Chen, K. Luo, J. Xu, D. Zhou, F. Wu, Environ. Sci. Technol. 21 (2017) 12663–12671.
[70] L. Chen, X. Zuo, S. Yang, T. Cai, D. Ding, Chem. Eng. J. 359 (2019) 373–384.
[71] N.S. Shah, J.A. Khan, M. Sayed, Z.U.H. Khan, A.D. Rizwan, N. Muhammad, G. Boczkaj, B. Murtaza, M. Imran, H.M. Khan, G. Zaman, Chem. Eng. J. 351 (2018) 841–855.
[72] M. Chen, W. Chu, Appl. Catal. B 168-169 (2015) 175–182.
[73] G. Wang, D. Zhao, F. Kou, Q. Ouyang, J. Chen, Z. Fang, Chem. Eng. J. 351 (2018) 747–755.
[74] D. Ding, C. Liu, Y. Ji, Q. Yang, L. Chen, C. Jiang, T. Cai, Chem. Eng. J. 308 (2017) 330–339.